

# Self-Doping of the Transport Layers Decreases the Bimolecular Recombination by Reducing Static Disorder

Elifnaz Sağlamkaya, Seyed Mehrdad Hosseini, Nurlan Tokmoldin, Artem Musiienko, Thomas Krüger, Jan Behrends, Meysam Raoufi, Dieter Neher, and Safa Shoaee\*

Electron-transport layers (ETLs) have a crucial role in the solar cells' performance. Generally, ETLs are characterized in terms of the interface properties and conductivity rather than their effect on the photoactive layer. Herein, two ETLs, 2,9-bis(3-((3-(dimethylamino)propyl)amino)propyl)anthra[2,1,9-*def*:6,5,10-*d'* *e'* *f'*]diisoquinoline-1,3,8,10(2*H*,9*H*)-tetraone (PDINN) and 2,9-bis[3-(dimethyloxidoamino)propyl]anthra[2,1,9-*def*:6,5,10-*d'* *e'* *f'*]diisoquinoline-1,3,8,10(2*H*,9*H*)-tetrone, are compared in the conventional PM6:Y6 organic solar cell (OSC) structure and the influence of the ETL on the photoactive layer is shown. It is shown that a significant portion of the unpaired electrons of PDINN is mobile by combining electron paramagnetic resonance and Hall effect measurements. It is established that the high doping in PDINN ETL changes the dark electron concentration of the photoactive layer. The impacts of this change in the photoactive layer can be observed in the reduced static energetic disorder, and subsequently in the (nonradiative) recombination of free carriers. The results can be used to suppress nonradiative recombination in OSC, which can significantly boost their efficiency.

## 1. Introduction

Organic solar cells (OSCs) are continuing to achieve new breakthroughs in performance, with new molecular designs of non-fullerene acceptors (NFA). NFA active materials are developing rapidly with new insights on the working mechanism of bulk heterojunctions. However, the development of the transport layers and their effect on the electronic properties of the active layer is not yet thoroughly understood, in particular how transport layers can affect not just surface recombination but also the bulk recombination in the active layer. The recombination of free charge carriers in OSCs proceeds through the decay of the charge transfer (CT) states. The decay is either radiative or nonradiative, with nonradiative pathways typically dominating because of a low CT to ground state oscillator strength. Reducing the

recombination is paramount to achieve high fill factors (FFs), in particular in thick junctions, while simultaneously improving open-circuit voltage ( $V_{OC}$ ). Furthermore, nonradiative recombination has been linked to energetic disorder of the organic photoactive layer.<sup>[1,2]</sup> As such, transport layers are important to mitigate all loss channels both in the bulk and interfaces.


Transport layers are employed to better the electrode work function (WF) with the active layer's energetics, reduce the energy barriers at the interfaces, and block the collection of the opposite type of charge carriers.<sup>[3,4]</sup> Perylene diimide (PDI) derivatives with various functional groups have been commonly employed as electron acceptor materials in the bulk heterojunction,<sup>[5]</sup> but also serve as electron-transport layers (ETLs) due to their favorable energetic contact with the organic active layers.<sup>[6,7]</sup> Especially for the NFA-based systems, PDI-based ETLs are quite popular due to good surface quality.<sup>[8]</sup> There is a wide variety of the of them with self-doped character.<sup>[6]</sup> A self-doped material is defined as a molecule with ionizable groups covalently attached to its conductive core.<sup>[9]</sup> Self-doping enhances the electronic conductivity<sup>[10,11]</sup> without the drawbacks of the extrinsic doping such as demixing, poor diffusivity, and aggregation of the dopants.<sup>[12]</sup> As an example, *N*-oxide bearing 2,9-bis[3-(dimethyloxidoamino)propyl]anthra[2,1,9-*def*:6,5,10-*d'* *e'* *f'*]diisoquinoline-1,3,8,10(2*H*,9*H*)-tetrone (PDINO) is a self-doped ETL. It has been demonstrated to have Ohmic contact when used with poly[[4,8-bis[5-(2-ethylhexyl)-4-fluoro-2-thienyl]

E. Sağlamkaya, S. M. Hosseini, N. Tokmoldin, S. Shoaee  
Disordered Semiconductor Optoelectronics  
Institute of Physics and Astronomy  
University of Potsdam  
Karl-Liebknecht-Str. 24-25, 14476 Potsdam-Golm, Germany  
E-mail: shoai@uni-potsdam.de

A. Musiienko  
Department Novel Materials and Interfaces for Photovoltaic Solar Cells  
Helmholtz-Zentrum Berlin für Materialien und Energie  
Albert-Einstein-Straße 16, 12489 Berlin, Germany

T. Krüger, J. Behrends  
Berlin Joint EPR Lab and Institut für Experimentalphysik  
Freie Universität Berlin  
14195 Berlin, Germany

M. Raoufi, D. Neher  
Soft Matter Physics and Optoelectronics  
Institute of Physics and Astronomy  
University of Potsdam  
Karl-Liebknecht-Str. 24-25, 14476 Potsdam-Golm, Germany

 The ORCID identification number(s) for the author(s) of this article can be found under <https://doi.org/10.1002/solr.202300423>.

© 2023 The Authors. Solar RRL published by Wiley-VCH GmbH. This is an open access article under the terms of the Creative Commons Attribution License, which permits use, distribution and reproduction in any medium, provided the original work is properly cited.

DOI: 10.1002/solr.202300423

benzo[1,2-*b*:4,5-*b'*]dithiophene-2,6-diyl]-2,5-thiophenediyl][5,7-bis(2-ethylhexyl)-4,8-dioxo-4*H*,8*H*-benzo[1,2-*c*:4,5-*c'*]dithiophene-1,3-diyl]-2,5-thiophenediyl]:2,2'-[[12,13-bis(2-ethylhexyl)-12,13-dihydro-3,9-diundecylbisthieno[2'',3'':4',5']thieno[2',3':4,5]pyrrolo[3,2-*e*:2',3'-*g*][2,1,3]benzothiadiazole-2,10-diyl]bis[[methylidyne(5,6-difluoro-3-oxo-1*H*-indene-2,1(3*H*)-diylidene)]bis[propanedinitrile] (PM6:Y6) system without significant surface recombination.<sup>[13]</sup> An alternative for the PDINO ETL named 2,9-bis(3-(3-(dimethylamino)propyl)amino)propyl) anthra[2,1,9-*def*:6,5,10-*d'e'f'*]diisoquinoline-1,3,8,10(2*H*,9*H*)-tetraone (PDINN) was synthesized and investigated by Yao et al.<sup>[14]</sup> Instead of the *N*-oxide groups, this PDI derivative has aliphatic amine groups. The authors reported increased FF,  $V_{OC}$ , and power conversion efficiency (PCE) of the regular PM6:Y6 devices when using PDINN instead of PDINO.<sup>[14]</sup> This was explained by the increased conductivity of the ETL and the WF modification of the metal electrodes.<sup>[14–16]</sup> However, when applied to PM6:Y6, the energy levels and WF of PDINO appear as a better match. In addition, in contrast to general expectation, reducing the thickness of ETL—for both PDINO and PDINN—resulted in better device performance,<sup>[14]</sup> which is in discord with the high conductivity of PDINN and questions the significance of increased conductivity. This discrepancy raises the question of the underlying mechanism behind the improved performance with PDINN.

In this work, we investigate the effect of PDINN and PDINO on the optoelectronic PM6:Y6 processes determining the device performance of solution-processed PM6:Y6 with two different active layer thicknesses of 100 and 200 nm. Consistent with previous publication,<sup>[14]</sup> both thin and thick junction PM6:Y6 devices with PDINN perform better than their PDINO counterpart. From electron paramagnetic resonance (EPR) and Hall effect experiments, we confirm that PDINN has a significantly higher dark electron concentration. By conducting a range of electrical and optoelectronic experiments, we establish correlations between energetic disorder of the active layer, the bimolecular recombination coefficient ( $k_{rec}$ ), the nonradiative voltage loss ( $\Delta V_{nr}$ ), and the FF. Our experiments show that the highly doped ETL, PDINN, reduces the (static) energetic disorder of the active layer, which results in reduced recombination of free charge carriers and voltage losses. Based on these findings, we postulate that the reduction of the energetic disorder is due to the charging of the acceptor at the interface with the self-doped ETL. We find that despite PDINO having more favorable energetics, the photoactive layer in PDINN device has lower energetic disorder and nonradiative recombination coefficient. The slower recombination results in higher FF and overall performance.

## 2. Results

### 2.1. Current–Voltage Characteristics

As the first step, we highlight the effect of ETL on the OSC performance by analyzing the conventional PM6:Y6 (1:1.2) devices in the ITO/PEDOT: PSS (30 nm)/PM6:Y6(100 nm)/ETL (15 nm)/Ag (100 nm) structure, using PDINO and PDINN for the ETL. The chemical structures of the ETLs and the current density–voltage ( $J$ – $V$ ) characteristics are shown in **Figure 1**. The 100 nm junction device with PDINO ETL has 14.4% PCE

whereas the use of PDINN as the ETL improves the PCE to 17.0% (Figure 1b). The enhanced device performance mainly stems from an increase of the FF from 70.5% to 75.0% and the enhancement of  $V_{OC}$  from 0.80 V to 0.83 V. Similarly, the 200 nm-thick junction device shows improvement in the PCE from 10.7% to 11.7% upon switching from PDINO to PDINN (Figure S1a, Supporting Information). Again, the enhancement originates primarily from an increase in the FF from 54.3% to 59.5% (Table 1).

### 2.2. Doping

Both PDINN and PDINO exhibit a self-doping character. These molecules have the same electron-deficient conjugated core; while PDINO has *N*-oxide groups, PDINN has secondary and tertiary amine groups tethered to the PDI units. The *N*-oxide groups of PDINO have negative charge on the oxygen atom and the secondary amine groups of PDINN have a lone pair of electrons on the nitrogen atom (Figure 1a); self-doping mechanism is activated via electron transfer from these functional groups to the PDI core.<sup>[17]</sup> In order to compare their unpaired spin density, we perform EPR measurements. EPR data for films are shown in Figure 1c. The ETLs have the same isotropic *g*-values (2.0032), which indicates that the environments of the unpaired electrons are similar. However, the signal for the PDINN is asymmetric, which may arise from an asymmetric *g* tensor or interactions between neighboring spins. The calculated spin density for the PDINO film is  $5 \times 10^{18} \text{ cm}^{-3}$ . However, for the PDINN film, the spin density is  $2.3 \times 10^{19} \text{ cm}^{-3}$  which is 4.6 times higher (see Note S1, Supporting Information).

We further probe the density of the free charges in the ETLs with Hall effect measurements. In the 4-probe geometry Hall effect setup, the voltage between the Hall contacts ( $U_H$ ) and the current ( $I$ ) between the fixed gate ( $V_G$ ) and source and drain ( $V_{SD}$ ) voltages are measured over time upon application of a perpendicular magnetic field ( $B_H$ ). The sign of the  $U_H$  reveals the type of the dominant charge carriers, which are *n*-type in our case. The charge carrier density is calculated from the ratio of the  $B$  to  $U_H$  ( $n = B \times I / (e U_H D)$ ), where  $e$  is the elementary charge,  $I$  is an electrical current, and  $D$  is the material thickness.<sup>[18]</sup> Hall effect is selective to the mobile charge carriers that move via band-like transportation and enable estimation of trap-free mobility.<sup>[19]</sup> The mobile electron density of the 100 nm PDINO film is estimated as  $2 \times 10^{17} \text{ cm}^{-3}$  and of the PDINN film as  $6 \times 10^{18} \text{ cm}^{-3}$ . Hall effect measurements also confirm a significant difference between the doping level of PDINN and PDINO. On the other hand, these values are lower compared to the ones we get with EPR. That is presumably because, among all of the unpaired spins detected with EPR, only a fraction is able to drift when  $B_H$  is applied during the Hall measurements. Moreover, comparison of these two measurements shows that the 26% of the spin density in the PDINN is mobile, whereas only the 4% of the unpaired electrons of the PDINO is mobile.

To evaluate whether the ETL doping affects the properties of the active layer, we performed capacitance–voltage ( $C$ – $V$ ) measurements on the devices without an ETL, and with two different ETLs: PDINO and PDINN. In order to accurately estimate the doping density with the Mott–Schottky (MS) analysis, one has

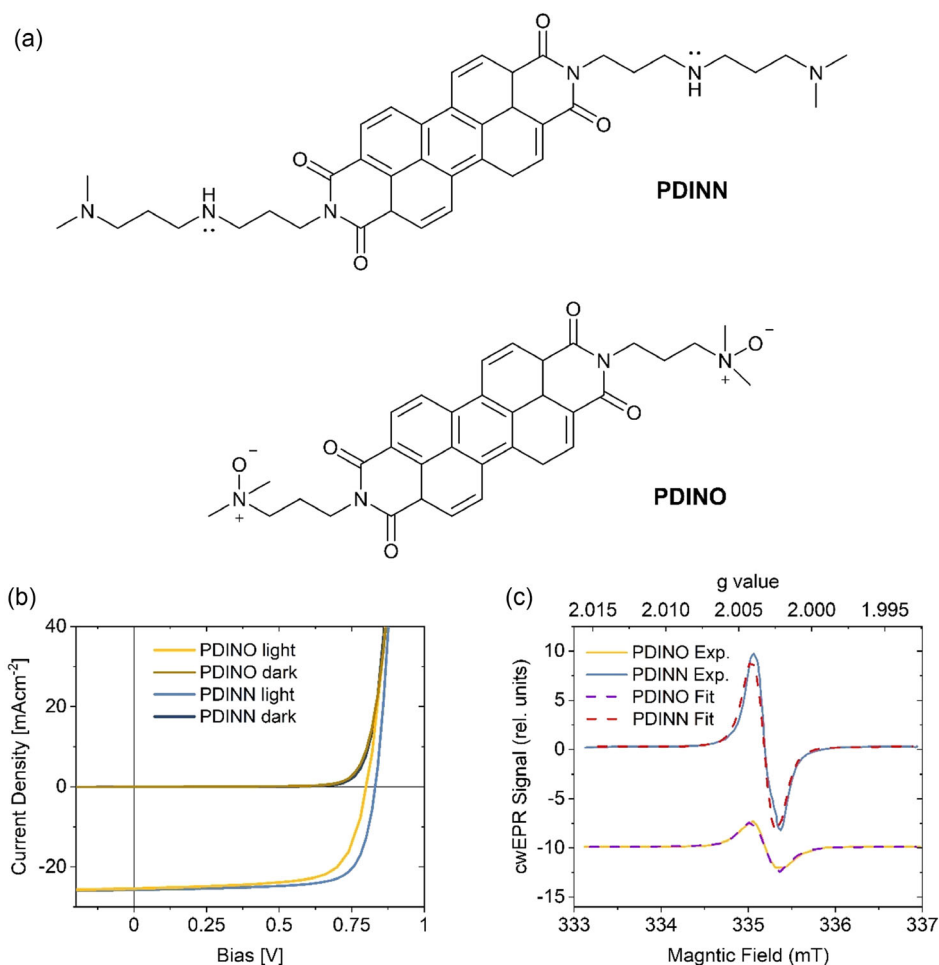


**Figure 1.** Effect of the choice of the ETL on solar cell efficiency and the strength of the self-doping. a) Chemical structures of the PDINN and PDINO. b)  $J$ - $V$  characteristics of the regular PM6:Y6 devices with 100 nm active layer thickness, with PDINN and PDINO ETL under simulated AM1.5 conditions. c) The EPR spectra of the PDINN and PDINO films.

**Table 1.** Device characteristics for champion 100 and 200 nm junction PM6:Y6 devices with the two different ETLs under simulated AM1.5 conditions.

Device	$J_{sc}$ [mA cm <sup>-2</sup> ]	$V_{oc}$ [V]	FF [%]	PCE [%]
100 nm with PDINN	25.7	0.83	75.0	17.0
100 nm with PDINO	25.4	0.80	70.5	14.4
200 nm with PDINN	24.0	0.81	59.5	11.7
200 nm with PDINO	24.2	0.80	54.3	10.7

to consider the accumulated charge on the electrodes ( $CV_{bi}/eV$ ) which can be injected into the active layer, where  $C$  is the capacitance,  $V_{bi}$  is the built-in voltage,  $e$  is the elementary charge, and  $V$  is the volume. This capacitance here is the geometric capacitance ( $C_g = \epsilon_0 \epsilon_r A/d$ ), where  $\epsilon_0$  is the vacuum permittivity,  $\epsilon_r$  is the relative permittivity,  $A$  is the area, and  $d$  is the thickness.<sup>[20]</sup> If the  $CV_{bi}$  charge is the same with the carrier density that is calculated from the slope of the MS plot in the forward bias, then it is no

longer possible to estimate the actual doping density. We first calculated the  $CV_{bi}$  charge to be  $1.2 \times 10^{15} \text{ cm}^{-3}$ . We used high active layer thickness of 400 nm in order to accurately estimate the doping density.<sup>[21,22]</sup> Our MS analysis on the device with no ETL shows typical undoped behavior, with an upper limit for doping of  $1.2 \times 10^{15} \text{ cm}^{-3}$ .<sup>[21,23]</sup> The doping density of the device with PDINO ETL is twice as much of this limit,  $2.4 \times 10^{15} \text{ cm}^{-3}$ , and significantly higher for the device with PDINN ETL,  $5.6 \times 10^{15} \text{ cm}^{-3}$  (Figure S2, Supporting Information) highlighting the significant influence of ETL on the carrier concentration in the active layer. These measurements were repeated with another active layer thickness of 300 nm, and similar values are obtained for both transport layers (Figure S3, Supporting Information).

### 2.3. Charge Transport

The devices with PDINN ETL had consistently higher FF compared to the ones with PDINO. To explain this improvement, we note that the FF considers all field-dependent loss processes in an

illuminated cell. Thus, it is affected by a number of competing scenarios taking place throughout the lifecycle of photogenerated carriers: 1) formation of a CT state at the interface of the donor (D) and the acceptor (A), which competes with the exciton decay to the ground state; 2) CT dissociation into free charges, which competes with their geminate recombination; and 3) collection of free charges, which competes with their nongeminate recombination. In efficient devices, it is in general assumed that exciton and CT dissociation (charge generation) are field-independent.<sup>[24]</sup> For such systems, including PM6:Y6, thus charge recombination versus extraction determines the FF losses.<sup>[25]</sup>

We start by examining the transport and extraction efficiency of the complete devices. Utilizing temperature-dependent space charge limited current (SCLC) studied electron mobilities,  $\mu_e$ , and hole mobilities,  $\mu_h$ , by preparing single carrier devices.

The measured current–voltage curves for electron-only devices are shown in **Figure 2**. The solid line demonstrates the fits according to the Murgatroyd–Gill model, which allows us to determine the zero-field mobility ( $\mu_0$ ) for electrons and holes. We estimated the zero-field mobility from the region, where the slope of the dark  $J$ – $V$  in the double log scale is equal to 2 using Equation (1) introduced by Murgatroyd.

$$J = \frac{9}{8} \epsilon_r \epsilon_0 \mu_0 \frac{(V - V_{bi})^2}{L^3} \exp\left(0.891\gamma \sqrt{\frac{V - V_{bi}}{L}}\right) \quad (1)$$

where  $L$  is the device thickness,  $V_{bi}$  is the built-in voltage,  $\mu_0$  is the zero-field mobility,  $\epsilon_r$  and  $\epsilon_0$  are relative and vacuum permittivities, and  $\gamma$  is the field-enhancement factor.<sup>[26]</sup> Hole-only devices were fabricated in ITO/MoO<sub>x</sub>/PM6:Y6/MoO<sub>x</sub>/Ag configuration, and gave a  $\mu_h$  of  $5.5 \times 10^{-4} \text{ cm}^2 \text{ V}^{-1} \text{ s}^{-1}$ . The mobility of the electron-only devices with different ETLs is given in **Table 2**.

In disordered semiconductors, the molecules have a distribution of energy levels due to the different structural conformations and imperfect crystallinity. Using the Gaussian disorder model (GDM), which assumes that the energy levels of these molecules have a Gaussian distribution, energetic disorder ( $\sigma_{\text{LUMO}}$ ) and ( $\sigma_{\text{HOMO}}$ ) of the lowest unoccupied molecular orbital (LUMO) of the A and the highest occupied molecular orbital (HOMO) of the D, respectively, can be determined as the standard

**Table 2.** The zero field SCLC electron mobility values ( $\mu_e$ ) are calculated from Murgatroyd–Gill equation and the energetic disorder ( $\sigma_{\text{LUMO}}$ ) is estimated with the temperature-dependent measurements for the electron-only devices with PDINN and PDINO as the one ETL.

ETL	$\mu_e$ [ $\text{cm}^2 \text{ V}^{-1} \text{ s}^{-1}$ ]	$\sigma_{\text{LUMO}}$ [eV]
PDINN	$5.4 \times 10^{-4}$	59
PDINO	$4.8 \times 10^{-4}$	65

deviation ( $\sigma$ ) of the Gaussian curve. GDM model allows us to determine  $\sigma$  from the temperature dependency of  $\mu_0$  using Equation (2).<sup>[27]</sup>

$$\mu_0(T) = \mu^* \exp\left(-c_2 \left(\frac{\sigma}{k_B T}\right)^2\right) \quad (2)$$

where  $\mu^*$  is the mobility at infinite temperature,  $k_B T$  the thermal energy, and  $c_2$  is the fitting parameter. In the GDM, the value of this parameter is 0.44, according to previous studies.<sup>[27]</sup>

The  $\sigma_{\text{HOMO}}$  of the hole-only PM6:Y6 device is estimated to be 78 meV (Figure S4, Supporting Information). We observe that the electron-only device with PDINN ETL, compared to PDINO, exhibits a reduced  $\sigma_{\text{LUMO}}$  ( $\Delta\sigma_{\text{LUMO}} = 6 \text{ meV}$ ). However, we note that the  $\mu_e$  of the blend doesn't change too much by changing the ETL, which indicates that the better extraction with the PDINN ETL is not the sole reason of the improved performance.

## 2.4. Recombination

To understand the competition between extraction versus recombination, we investigate the recombination coefficient of photo-generated charge carriers through performing bias-assisted charge extraction (BACE) measurements (**Figure 3a**) (more details on the method are in Note S2, Supporting Information). As shown in Figure 3a, both systems exhibit recombination coefficient,  $k_{\text{rec}}$ , fairly independent of the carrier density—indicative of second-order kinetics, that is, a recombination rate of the form  $R = k_{\text{rec}} n^2$ , where  $n$  is the carrier density. While we note that the active layer is the same in both systems, yet we observe

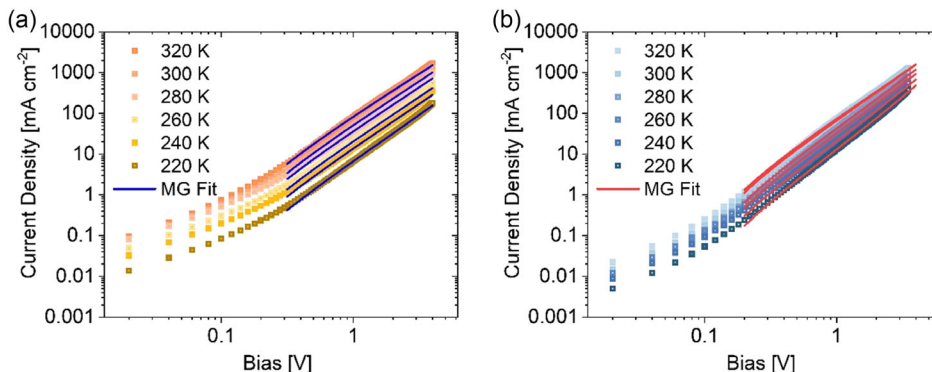


**Figure 2.** The SCLC versus voltage curves of the single carrier devices with a 150 nm active layer thickness in the configuration ITO/ZnO/PM6:Y6/ETL/Ag and a) 15 nm PDINO or b) PDINN as the ETL, measured at different temperatures. The fits were made using the Murgatroyd–Gill equation as shown by straight lines.



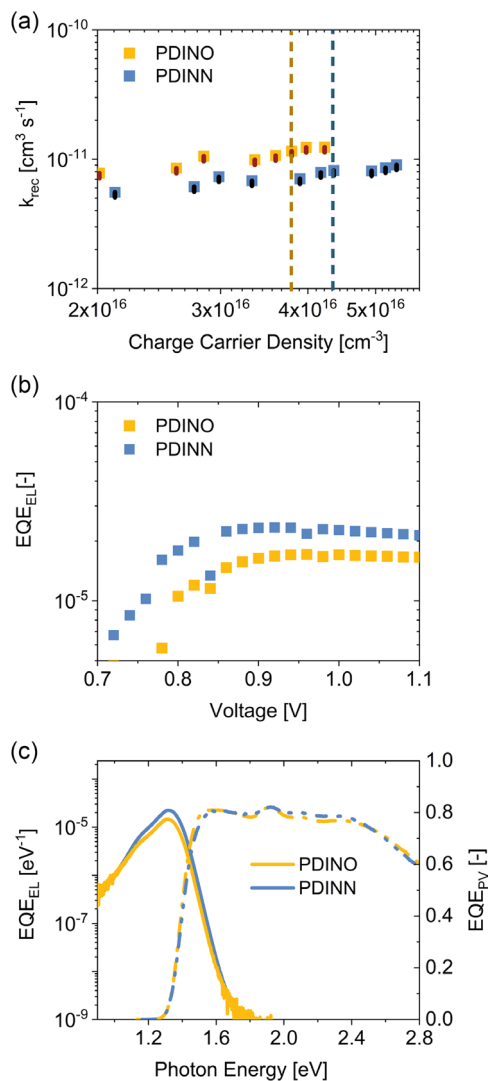


**Figure 3.** a) Bimolecular recombination coefficient as a function of charge carrier density, obtained from BACE measurements for PM6:Y6 with 100 nm active layer thickness shown together with the error bars. The dark yellow vertical dashed line corresponds to the measurement point at 1 sun intensity of the device with PDINO and the blue one belongs to the device with PDINN. b) The  $\text{EQE}_{\text{EL}}$  for different injection currents measured by a Si photodiode as a function of the applied bias. c) The spectral  $\text{EQE}_{\text{EL}}$  for the injection current that corresponds to the device  $J_{\text{SC}}$  at 1 sun condition, left axis, and photovoltaic external quantum efficiency  $\text{EQE}_{\text{PV}}$ , right axis, of the 100 nm of PM6:Y6 devices with PDINN and PDINO as ETL.

different  $k_{\text{rec}}$  values for the two different ETL devices. For PM6:Y6 blend,  $k_{\text{rec}}$  decreased from  $1 \times 10^{-11} (\pm 1.2 \times 10^{-13})$  to  $8 \times 10^{-12} (\pm 4.0 \times 10^{-14}) \text{ cm}^3 \text{ s}^{-1}$  by changing the ETL from PDINO to PDINN (Figure 3a). The error was calculated from the typical standard deviation of the collected charge in a BACE measurement. Previous work has shown negligible interfacial recombination for PM6:Y6 with PDINO and PEDOT:PSS transport layers, and concluded the main recombination originates from the bulk.<sup>[13]</sup> Therefore, the suppression of  $k_{\text{rec}}$  reported herein is most likely to be occurring in the bulk. Recent work has shown recombination, more specifically the

nonradiative channel, can be suppressed by decreasing the energetic disorder of the CT states.<sup>[2,28–30]</sup> Therefore, we consider the suppressed recombination in the active layer to originate from the reduced energetic disorder. This hypothesis is supported by the previous study by Yan et al., showing the relationship between static disorder and nonradiative voltage losses ( $\Delta V_{\text{OC, nr}}$ ).<sup>[11]</sup> Employing electroluminescence (EL) technique for 100 nm-thick devices measured at 1 sun condition, we calculate the nonradiative voltage loss ( $\Delta V_{\text{OC, nr}}$ ) using the relation,  $q\Delta V_{\text{OC, nr}} = -k_{\text{B}}T \ln(\text{EQE}_{\text{EL}})$ .<sup>[31]</sup> The external EL quantum efficiency ( $\text{EQE}_{\text{EL}}$ ) was calculated by measuring the emitted photons with a silicon photodiode as a function of injection bias, as shown in Figure 3b.

For the same injection current, the PDINN device is slightly more emissive, as seen from EL spectra in Figure 3b. The  $\text{EQE}_{\text{EL}}$  of the devices with PDINN is higher, corresponding to  $\Delta V_{\text{OC, nr}}$  of 0.30 eV, while the use of PDINO as an ETL has a loss of 0.32 eV. To calculate the radiative limit for the  $V_{\text{OC}}$ , we convoluted the spectrally resolved photovoltaic external quantum efficiency ( $\text{EQE}_{\text{PV}}$ ) with the black body photon flux. Figure 3c shows the  $\text{EQE}_{\text{PV}}$  for both devices on the right axis. The switch to PDINN from PDINO does not change the shape of the  $\text{EQE}_{\text{PV}}$ , and their low energy tails completely overlap, and found the radiative limit for the  $V_{\text{OC}}$  to be 1.09 eV for both of the ETLs. As such we conclude the reduced nonradiative voltage loss is the origin of the slightly increased  $V_{\text{OC}}$  in PDINN device due to reduced recombination.<sup>[2]</sup>

## 2.5. Simulation

To elucidate and confirm the influence of the active layer doping density, charge carrier mobility, and the  $k_{\text{rec}}$  in full OSC devices, we employed drift-diffusion simulations to model the devices using our measured mobilities and recombination coefficients. Figure 4a shows the experimental and simulated  $J$ - $V$  curves. Introducing an n-type dopant into the active layer increases the electron carrier mobility, and decreases the recombination coefficient of the free carriers which results in higher FF and a slight shift of the  $J$ - $V$  curve to a higher  $V_{\text{OC}}$ . A list of input parameters is provided in Table S2, Supporting Information. To further confirm our findings on recombination versus extraction competition, we employed the analytical figure of merit proposed by Neher et al.<sup>[32]</sup> to predict the FF from a unitless parameter, which contains information on the transport and recombination properties of the active layer using Equation (3).

$$\alpha^2 = \frac{q^2 k_{\text{rec}} G d^4}{4 \mu_e \mu_h (k_{\text{B}} T)^2} \quad (3)$$

where  $q$  is the elementary charge,  $G$  is the generation rate,  $d$  is the active layer thickness,  $k_{\text{B}}$  is the Boltzmann constant, and  $T$  is the temperature in Kelvin.

$$\text{FF} = \frac{u_{\text{OC}} - \ln(0.79 + 0.66u_{\text{OC}}^{1.2})}{u_{\text{OC}} + 1} \quad (4)$$

where  $u_{\text{OC}}$  is the normalized  $V_{\text{OC}}$

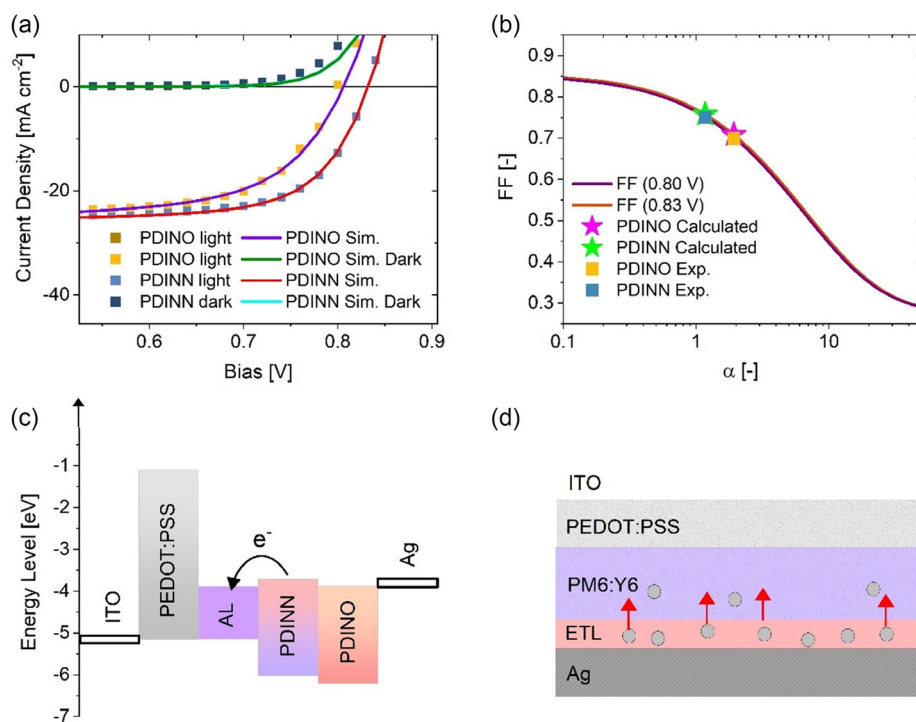


**Figure 4.** Drift-diffusion and analytical simulations. a) Simulated curves of the PM6:Y6 devices with PDINN ETL ( $V_{OC} = 0.83$  V,  $J_{SC} = 25.7$  mA cm<sup>-2</sup>, FF = 75.7%) and with PDINO ETL ( $V_{OC} = 0.80$  V,  $J_{SC} = 25.5$  mA cm<sup>-2</sup>, FF = 69.8%) with structure ITO/PEDOT:PSS/PM6:Y6/ETL/Ag (fully reflecting 100 nm) under simulated AM1.5G light. Open squares are the experimental results and the solid lines are the drift-diffusion simulation results generated using the experimentally determined values for  $k_{rec}$  and  $\mu_{e/h}$ . b) The unitless alpha parameter was calculated with Equation (3), using the experimental values for the mobility, bimolecular recombination,  $V_{OC}$ , and generation rate, and the FF was estimated using the Equation (4) and (5).<sup>[39]</sup> Solid lines correspond to the theoretical FFs for given  $V_{OC}$  and a range of  $\alpha$  values, and the star symbols correspond to the calculated data. c) The energy levels of the full stack of the device. d) Schematic representation of the CT from ETL to the active layer.

$$u_{OC} = \frac{qV_{OC}}{(1 + \alpha)k_B T} \quad (5)$$

Figure 4b demonstrates the experimentally determined FF at AM1.5G illumination for both ETLs as a function of  $\alpha$ . Also plotted on the same figure is the calculated values of the FF for each system based on the approach presented by Neher using Equation (4) and (5).<sup>[32]</sup> As can be seen from Figure 4b, indeed the slight improvement in the FF can be explained by the reduced bimolecular recombination losses and the increased charge carrier mobility.<sup>[33]</sup>

### 3. Discussion

From our Hall measurement and MS data, we see a correlation between the doping density of the ETL and the carrier density in the active layer. This indicates a charge spilling mechanism taking place near the ETL/active layer interface. Wu et al. have shown that the amine groups of a naphthalene diimide-based, self-doped, n-type water/alcohol-soluble conjugated ETL increase the doping-level PC<sub>71</sub>BM acceptor in the active layer, leading to enhanced device performance via charge spilling.<sup>[34,35]</sup> Another example of charge spilling from the ETL was reported by Kang

et al. where the electrons of the amine groups of poly[(9,9-bis(3-(N,N-dimethylamino)propyl)-2,7-fluorene)-alt-2,7-(9,9-dioctylfluorene)] (PFN) n-dopes the acceptor molecule, causing charge accumulation at the interface, this time reducing the performance.<sup>[36]</sup> The CT or the effective n-doping of the active layer by the ETL changes the device parameters such that non-geminate recombination within this region is reduced and extraction efficiency is improved, both manifested in gain in the  $V_{OC}$  and FF. Our experimental observation is confirmed by our drift-diffusion simulations which cannot reproduce the  $J$ - $V$  solely by changing the doping density or extraction versus recombination efficiency. On a similar note, the reported WF difference of the Ag/PDINO (3.88 eV) and Ag/PDINN (3.72 eV)<sup>[14]</sup> also does not reflect in the drift-diffusion simulations to give the measured  $V_{OC}$  increase. Indeed, given that increasing the energy offset did not reduce the  $V_{OC}$  (due to the reduction of the built-in voltage), the slight increase in  $V_{OC}$  can be due to reduced nonradiative voltage losses.

To connect the optoelectrical observations regarding the EQE<sub>EL</sub> of the active layer above with the doping concentration of the ETLs, we consider intermolecular electron transfer from PDINN to the active layer, which acts to reduce the energetic disorder of the active layer via trap state filling. This, in turn, has an effect on the decay of the CT state to the ground state. Hosseini

et al. have recently analyzed the correlation between energetic disorder and free charge recombination through the reformation and decay of the CT state.<sup>[2]</sup> The presented data herein support that nongeminate losses occur mainly through recombination of carriers situated in a Gaussian distribution of states, whose width is affected by CT of the adjacent ETL in contact. We see that the suppressed nonradiative decay of the CT state reduces the recombination, which is verified with  $\Delta V_{OC, nr}$  and  $k_{rec}$  measurements and our drift-diffusion simulations which fully reproduce the  $J$ - $V$  curves of the two devices.

## 4. Conclusion

In summary, we studied the performance of conventional PM6:Y6(1:1.2) devices with PDINO and PDINN ETLs. Mott-Schottky analysis suggests that the doping density of the transport layers alters the dark electron concentration in the active layer through a charge spilling effect. We also observed a difference in the energetic disorder of the active layer due to the trap filling, with PDINN showing smaller disorder. The reduced nonradiative recombination is a direct result of this suppressed energetic disorder. This plays a role in enhancing both the FF and the  $V_{OC}$  and thus the overall performance. In conclusion, we show that the choice of the transport layers is relevant not only for the interface properties, but also the bimolecular recombination and the energetic disorder of the active layer.

## 5. Experimental Section

**Device Preparation:** PM6, Y6, PDINO, and PDINN were purchased from 1-Material Inc. Chloroform ( $\text{CHCl}_3$ ) and methanol were purchased from Sigma-Aldrich. Solvent additive 1-chloronaphthalene (CN) was purchased from Alfa Aesar. PEDOT:PSS (poly(3,4-ethylenedioxythiophene):poly(styrene sulfonate)) Baytron PVP Al 4083 was purchased from Heraeus. The devices with a regular configuration were fabricated with a structure of ITO/PEDOT:PSS/PM6:Y6/ETL/Ag. Patterned ITO (Lumtec & PsiOTech Ltd.) substrates were cleaned in a beaker with Hellmanex at 75 °C for 1 h, wiped with paper tissues, and then taken to an ultrasonic bath to proceed to the cleaning with Hellmanex for 20 min, deionized water for 20 min, acetone for 15 min, and isopropanol for 15 min, followed by microwave plasma treatment (4 min at 200 W). PEDOT:PSS was filtered and spin-coated onto ITO at 5000 rpm and annealed at 150 °C for 15 min. Blend solutions were prepared with 0.5% CN (v/v, CN/ $\text{CHCl}_3$ ) in 16 mg  $\text{mL}^{-1}$  concentration. 100 nm of the active layer was spin-coated onto hole-transport layer at 1700 rpm and annealed at 110 °C for 10 min. ETLs were spin-coated onto the active layer from 1 mg  $\text{mL}^{-1}$  methanol solution at 1000 rpm and Ag electrodes were evaporated under a  $10^{-6}$ – $10^{-7}$  mbar vacuum.

**Current–Voltage Characteristics:**  $J$ - $V$  curves were measured using a Keithley 2400 system in a 2-wire source configuration. Simulated AM1.5G irradiation at 100  $\text{mWcm}^{-2}$  was provided by a filtered Oriol Class AAA Xenon lamp and the intensity was monitored simultaneously with a Si photodiode. The sun simulator is calibrated with a KG5 filtered silicon solar cell (certified by Fraunhofer ISE).

**EPR:** PDINO and PDINN samples for quantitative EPR measurements were prepared by dissolving the respective materials in methanol at a concentration of 5 mg  $\text{mL}^{-1}$  and filling 60  $\mu\text{L}$  of the solutions into 3 mm inner-diameter quartz tubes inside a nitrogen atmosphere glove box. The solvent was then evaporated under vacuum, resulting in a solid film on the inner walls of the EPR tubes. The tubes were backfilled with helium and flame-sealed to prevent degradation.

Room-temperature X-band continuous wave EPR measurements were carried out using an ER 4122 SHQE resonator on a laboratory-built

spectrometer consisting of a Bruker ER 041 MR microwave bridge with an ER 048R microwave controller, an AEG electromagnet with a Bruker BH15 Hall effect field controller, and using a Stanford Research SR810 lock-in amplifier with a Wangine WPA-120 modulation amplifier for field modulation and lock-in detection. The spectra were acquired at a microwave frequency of 9.40 GHz and a microwave power of 200  $\mu\text{W}$  (well below saturation) with 100 kHz modulation frequency and modulation amplitudes between 0.08 and 0.10 mT. The magnetic field was calibrated with a standard N@C60 sample with a known  $g$ -value. The quality factor of the resonator was determined from the mode picture for each measurement and used for the quantitative analysis. The spectrometer was calibrated for spin quantitation with a reference sample of TEMPO in toluene with a known concentration. The spin concentration for PDINO and PDINN was determined from the double integrals of the recorded EPR spectra.

**Capacitance–Voltage Measurements:** The dark  $C$ - $V$  measurements were performed using the Keysight E5061B Vector Network Analyzer with the frequency measurement range of 5 Hz to 500 MHz. Prior to the measurements, the tool was calibrated using the 85032E Type N calibration kit. This was followed by the tool compensation procedure using the “Open”, “Short”, and “50 Ohm” measurements at the device connection fixture. The measurements were performed in the  $C_p$  mode.<sup>[37]</sup> The performance of the devices was tested both prior to and after the  $C$ - $V$  measurements with no sign of degradation.

**SCLC:** Electron-only devices were prepared in ITO/ZnO/PM6:Y6 (170–200 nm)/ETL (15 nm)/Ag (100 nm) configuration. ZnO nanoparticle dispersion in isopropanol (Avantama N-10) was filtered with a 0.45  $\mu\text{m}$  polytetrafluoroethylene filter and spin-coated onto ITO at 5000 rpm for 40 s in air and annealed at 120 °C for 30 min. Hole-only devices with the configuration ITO/ $\text{MoO}_3$  (8 nm)/PM6:Y6(170–200 nm)/ $\text{MoO}_3$  (8 nm)/Ag (100 nm) and ITO/ $\text{MoO}_3$  (8 nm)/PM6:Y6(170–200 nm)/ $\text{MoO}_3$  (8 nm)/ETL/Ag (100 nm) were prepared by evaporating  $\text{MoO}_3$  on top of ITO. Then, the active layer was prepared as for solar cell devices, followed by evaporation of 8 nm of  $\text{MoO}_3$  under a  $10^{-6}$ – $10^{-7}$  mbar vacuum.

For temperature-dependent measurements, the devices were loaded into a liquid nitrogen-cooled cryostat (VFP-100 Janis) and the temperature was adjusted in a range of 220–320 K using a temperature controller (Lakeshore 335).  $J$ - $V$  data were measured using a Keithley 2400 Source Meter in a two-wire configuration.

**BACE:** In BACE, the devices were held at steady-state conditions by illumination with 1 W, 638 nm, and 520 nm laser diode (insaneware) with a switch-off time of  $\approx 10$  ns. The laser diode was operated at 500 Hz with a duty cycle of 50%, such that illumination lasted 1 ms and the diode was switched off for also 1 ms. Right after switching off the laser, a high reverse bias was applied to the sample by the same fast pulse generator (Agilent 81150A) allowing a fast extraction time of  $10^{-20}$  ns. The current transients were measured via a 10  $\Omega$  resistor in series with the sample and recorded with an oscilloscope (Agilent DSO9104H).

**$\text{EQE}_{EL}$  and Electroluminescence Spectra:** EL spectra were measured using a light guide positioned close to the sample. The voltage was applied using a Keithley 2400 Source Meter. The detector was a Newton EM-CCD Si array detector at  $-60$  °C with a Shamrock SR-303i spectrograph from Andor Tech.  $\text{EQE}_{EL}$  values of the 100 nm-thick devices were obtained from an in-house built system including a Hamamatsu silicon photodiode 1010B, a Keithley 2400 SourceMeter to apply the voltage and record the injected current that corresponds to the  $J_{SC}$  of the devices at 1 sun condition, and a Keithley 485 Picoammeter to measure the emitted light intensity.

**EQE:**  $\text{EQE}_{PV}$  was measured using a home-made setup containing a quartz tungsten halogen lamp, a Thorlabs MC2000B optical chopper at a frequency of 165 Hz, a Bentham TMC300 monochromator, a lock-in amplifier (SR830), and a preamplifier (SR570). The system was calibrated using a standard silicon detector from Enlitech.

**AC Hall Effect Measurements:** Hall effect with alternating field (AC Hall) measurements were conducted with an 8400 series of tools manufactured by Lake Shore Cryotronics and operated with 100 mHz and 0.6 T amplitude magnetic field. The conductivity, resistivity, carrier concentration, and Hall mobility parameters were directly measured using 4-probe Van der Pauw contact geometry. AC magnetical field and lock-in amplifier were used to enhance the Hall effect signal due to low mobility.

*1D Drift-Diffusion Simulations*: Online version of the open source simulation software named “SIMsalabim” was used for the  $J$ - $V$  simulations.<sup>[38]</sup>

## Supporting Information

Supporting Information is available from the Wiley Online Library or from the author.

## Acknowledgements

This work was supported in part by Deutsche Forschungsgemeinschaft (DFG, German Research Foundation, through the project Fabulous (project number 450968074) and the SFB HIOS (Projektnummer 182087777-SFB 951)). This project has received funding from the European Union's Framework Programme for Research and Innovation HORIZON EUROPE (2021–2027) under the Marie Skłodowska-Curie Action Postdoctoral Fellowships (European Fellowship) 101061809 HyPerGreen.

Open Access funding enabled and organized by Projekt DEAL.

## Conflict of Interest

The authors declare no conflict of interest.

## Data Availability Statement

The data that support the findings of this study are available from the corresponding author upon reasonable request.

## Keywords

electron-transport layers, fill factors, nonradiative recombination, perylene diimide, self-doping, static energetic disorder

Received: June 4, 2023

Revised: June 30, 2023

Published online: August 6, 2023

- [1] J. Yan, E. Rezasoltani, M. Azzouzi, F. Eisner, J. Nelson, *Nat. Commun.* **2021**, *12*, 3642.
- [2] S. M. Hosseini, S. Wilken, B. Sun, F. Huang, S. Y. Jeong, H. Y. Woo, V. Coropceanu, S. Shoaee, *Adv. Energy Mater.* **2023**, *13*, 2203576.
- [3] F. Jin, Z. Su, B. Chu, P. Cheng, J. Wang, H. Zhao, Y. Gao, X. Yan, W. Li, *Sci. Rep.* **2016**, *6*, 26262.
- [4] S. Li, Q. Fu, L. Meng, X. Wan, L. Ding, G. Lu, G. Lu, Z. Yao, C. Li, Y. Chen, *Angew. Chemie., Int. Ed.* **2022**, *61*, e202207397.
- [5] S. Shoaee, T. M. Clarke, C. Huang, S. Barlow, S. R. Marder, M. Heeney, I. McCulloch, J. R. Durrant, *J. Am. Chem. Soc.* **2010**, *132*, 12919.
- [6] Z. G. Zhang, B. Qi, Z. Jin, D. Chi, Z. Qi, Y. Li, J. Wang, *Energy Environ. Sci.* **2014**, *7*, 1966.
- [7] K. Jiang, F. Wu, H. Yu, Y. Yao, G. Zhang, L. Zhu, *J. Mater. Chem. A* **2018**, *6*, 16868.
- [8] R. Sorrentino, E. Kozma, S. Luzzati, R. Po, *Energy Environ. Sci.* **2021**, *14*, 180.
- [9] M. S. Freund, B. A. Deore, in *Self-Doped Conducting Polymers*, John Wiley & Sons, Ltd, Chichester, UK, **2007**, p. i.
- [10] H. Yano, K. Kudo, K. Marumo, H. Okuzaki, *Sci. Adv.* **2019**, *5*, 1.
- [11] H. Tang, Z. Liu, Y. Tang, Z. Du, Y. Liang, Z. Hu, K. Zhang, F. Huang, Y. Cao, *Giant* **2021**, *6*, 100053.
- [12] D. Powell, X. Zhang, C. I. Nwachukwu, E. J. Miller, K. R. Hansen, L. Flannery, J. Ogle, A. Berzansky, J. G. Labram, A. G. Roberts, L. Whittaker-Brooks, *Adv. Mater.* **2022**, *34*, 2204656.
- [13] L. Q. Phuong, S. M. Hosseini, O. J. Sandberg, Y. Zou, H. Y. Woo, D. Neher, S. Shoaee, *Sol. RRL* **2021**, *5*, 2000649.
- [14] J. Yao, B. Qiu, Z. G. Zhang, L. Xue, R. Wang, C. Zhang, S. Chen, Q. Zhou, C. Sun, C. Yang, M. Xiao, L. Meng, Y. Li, *Nat. Commun.* **2020**, *11*, 2726.
- [15] J. Wan, X. Fan, H. Huang, J. Wang, Z. Zhang, J. Fang, F. Yan, *J. Mater. Chem. A* **2020**, *8*, 21007.
- [16] J. Yao, S. Ding, R. Zhang, Y. Bai, Q. Zhou, L. Meng, E. Solano, J. A. Steele, M. B. J. Roeflaers, F. Gao, Z. G. Zhang, Y. Li, *Adv. Mater.* **2022**, *34*, 2203690.
- [17] B. Russ, M. J. Robb, B. C. Popere, E. E. Perry, C. K. Mai, S. L. Fronk, S. N. Patel, T. E. Mates, G. C. Bazan, J. J. Urban, M. L. Chabinyk, C. J. Hawker, R. A. Segalman, *Chem. Sci.* **2016**, *7*, 1914.
- [18] V. Podzorov, E. Menard, J. A. Rogers, M. E. Gershenson, *Phys. Rev. Lett.* **2005**, *95*, 226601.
- [19] H. T. Yi, Y. N. Gartstein, V. Podzorov, *Sci. Rep.* **2016**, *6*, 23650.
- [20] F. Peña-Camargo, J. Thiesbrummel, H. Hempel, A. Musienko, V. M. Le Corre, J. Diekmann, J. Warby, T. Unold, F. Lang, D. Neher, M. Stollerfoht, *Appl. Phys. Rev.* **2022**, *9*, 021409.
- [21] T. Kirchartz, W. Gong, S. A. Hawks, T. Agostinelli, R. C. I. MacKenzie, Y. Yang, J. Nelson, *J. Phys. Chem. C* **2012**, *116*, 7672.
- [22] A. Nigam, M. Premaratne, P. R. Nair, *Org. Electron.* **2013**, *14*, 2902.
- [23] E. J. Lous, P. W. M. Blom, L. W. Molenkamp, D. M. de Leeuw, *Phys. Rev. B* **1995**, *51*, 17251.
- [24] L. Perdígón-Toro, H. Zhang, A. Markina, J. Yuan, S. M. Hosseini, C. M. Wolff, G. Zuo, M. Stollerfoht, Y. Zou, F. Gao, D. Andrienko, S. Shoaee, D. Neher, *Adv. Mater.* **2020**, *32*, 1906763.
- [25] S. Shoaee, A. Armin, M. Stollerfoht, S. M. Hosseini, J. Kurpiers, D. Neher, *Sol. RRL* **2019**, *3*, 1900184.
- [26] N. Felekidis, A. Melianas, M. Kemerink, *Org. Electron.* **2018**, *61*, 318.
- [27] H. Bässler, *Phys. Status Solidi* **1993**, *175*, 15.
- [28] T. F. Hinrichsen, C. C. S. Chan, C. Ma, D. Paleček, A. Gillett, S. Chen, X. Zou, G. Zhang, H.-L. Yip, K. S. Wong, R. H. Friend, H. Yan, A. Rao, P. C. Y. Chow, *Nat. Commun.* **2020**, *11*, 5617.
- [29] X. K. Chen, D. Qian, Y. Wang, T. Kirchartz, W. Tress, H. Yao, J. Yuan, M. Hülsbeck, M. Zhang, Y. Zou, Y. Sun, Y. Li, J. Hou, O. Inganäs, V. Coropceanu, J. L. Bredas, F. Gao, *Nat. Energy* **2021**, *6*, 799.
- [30] S. Wilken, D. Scheunemann, S. Dahlström, M. Nyman, J. Parisi, R. Österbacka, *Adv. Electron. Mater.* **2021**, *7*, 2001056.
- [31] U. Rau, *Phys. Rev. B* **2007**, *76*, 085303.
- [32] D. Neher, J. Kniepert, A. Elimelech, L. J. A. Koster, *Sci. Rep.* **2016**, *6*, 24861.
- [33] S. M. Hosseini, N. Tokmoldin, Y. W. Lee, Y. Zou, H. Y. Woo, D. Neher, S. Shoaee, *Sol. RRL* **2020**, *4*, 2000498.
- [34] Z. Wu, C. Sun, S. Dong, X. F. Jiang, S. Wu, H. Wu, H. L. Yip, F. Huang, Y. Cao, *J. Am. Chem. Soc.* **2016**, *138*, 2004.
- [35] J. Jia, B. Fan, M. Xiao, T. Jia, Y. Jin, Y. Li, F. Huang, Y. Cao, *Macromolecules* **2018**, *51*, 2195.
- [36] Q. Kang, Q. Wang, C. An, C. He, B. Xu, J. Hou, *J. Energy Chem.* **2020**, *43*, 40.
- [37] I. Zonno, A. Martinez-Otero, J.-C. Hebig, T. Kirchartz, *Phys. Rev. Appl.* **2017**, *7*, 034018.
- [38] M. Koopmans, V. Corre, L. Koster, *J. Open Source Softw.* **2022**, *7*, 3727.
- [39] N. Tokmoldin, J. Vollbrecht, S. M. Hosseini, B. Sun, L. Perdígón-Toro, H. Y. Woo, Y. Zou, D. Neher, S. Shoaee, *Adv. Energy Mater.* **2021**, *11*, 2100804.